



Using DInSAR, airborne LiDAR, and archival air photos to quantify landsliding and sediment transport

Joshua J. Roering,¹ Laura L. Stimely,¹ Benjamin H. Mackey,¹ and David A. Schmidt¹

Received 3 August 2009; revised 1 September 2009; accepted 3 September 2009; published 15 October 2009.

[1] We demonstrate the ability of coupled remote sensing tools to characterize large, slow-moving landslides in the Eel River catchment, northern California. From a stack of ALOS interferograms, we identified 5 large (>1 km long) landslides that exhibited significant activity from February 2007 to February 2008. For the Boulder Creek earthflow, we used orthorectified air photos taken in 1964 and unfiltered airborne LiDAR flown in 2006 to map the displacement of trees growing on the landslide surface. Combining those displacement orientations with stacked DInSAR data, we observed average downslope velocities of 0.65 m yr^{-1} through the central transport zone of the landslide. Given landslide depth estimates, minimum sediment transport and denudation rates are estimated to be $4100 \text{ m}^3 \text{ yr}^{-1}$ and 1.6 mm yr^{-1} , respectively. Our results demonstrate the highly erosive role of large, slow-moving landslides in landscape evolution and suggest that the superposition of dense, ephemeral gully networks and rapidly moving zones within the landslide may facilitate delivery of slide-mobilized sediment into adjacent fluvial channels. **Citation:** Roering, J. J., L. L. Stimely, B. H. Mackey, and D. A. Schmidt (2009), Using DInSAR, airborne LiDAR, and archival air photos to quantify landsliding and sediment transport, *Geophys. Res. Lett.*, *36*, L19402, doi:10.1029/2009GL040374.

1. Introduction

[2] In mountainous landscapes, landsliding is the primary contributor of sediment to channel networks and thus influences channel profile evolution, aquatic habitat, and slope morphology. Spatially distributed estimates of landslide activity can be used with rainfall and sediment gauging data to inform mechanistic models of slide dynamics [Baum *et al.*, 1998] and sediment production calculations [Schwab *et al.*, 2008]. In steep, potentially unstable terrain, field-based monitoring of landslide movement tends to be highly localized, expensive, and logistically challenging, such that field sites featuring spatially and temporally extensive records of landslide are sparse [e.g., Malet *et al.*, 2002]. In contrast, regional landslide inventories and associated sediment budget calculations are typically based on infrequently-acquired air photo or remote sensing datasets that do not resolve landslide response to seasonal climate variation [e.g., Chandler and Brunsden, 1995; Guzzetti *et al.*, 2009; Hovius *et al.*, 1997; Korup *et al.*, 2007]. As a result, landslide studies tend to be local and highly detailed or spatially extensive with somewhat limited resolution.

¹Department of Geological Sciences, University of Oregon, Eugene, Oregon, USA.

[3] Differential Interferometric Synthetic Aperture Radar (DInSAR) and airborne laser altimetry (LiDAR) data have transformed our ability to quantify Earth surface processes at the meter scale. First, satellite-based radar interferometry has revolutionized our ability to measure mm-scale displacement of the Earth's surface, generating regional deformation maps associated with seismic and volcanic activity [Massonnet and Feigl, 1998]. DInSAR has been successfully used to measure landslide activity in some favorable settings [e.g., Bulmer *et al.*, 2006; Catani *et al.*, 2005; Hilley *et al.*, 2004], although results in mountainous regions have been limited because interferogram coherence can be poor in vegetated and steep terrain [Delacourt *et al.*, 2007; Squarzoni *et al.*, 2003]. The recent launch of the Japanese ALOS satellite, which operates an L-band SAR antenna, provides improved coherence in vegetated, mountainous environments compared to many C-band systems [Sandwell *et al.*, 2008]. Second, airborne LiDAR offers meter-scale characterization of topographic features, including vegetation as well as the bare Earth surface [Slatton *et al.*, 2007]. In the context of landslides, LiDAR facilitates accurate rectification of historical air photos as well as provides a template for mapping deformation and erosional features that cannot otherwise be resolved. Here, we describe a novel methodology that uses L-band ALOS DInSAR, airborne LiDAR, and historical air photos for estimating spatial and temporal variations in landslide activity and sediment delivery. Our results: (1) highlight the extent of active earthflows in our northern California field site along the Eel River, (2) reveal potential coupling between zones of rapid landslide transport and active gullying, and (3) provide a framework for pinpointing the timing and sources of sediment input that manifest in sediment gauging data.

2. Study Site: Eel River, Northern California

[4] The northern California coast range is comprised of the highly deformed meta-sedimentary Franciscan Mélange, a Jurassic-Cretaceous age accretionary prism complex renowned for earthflows and deep-seated landsliding [Kelsey, 1987]. Along the Eel River, which is underlain by Central Belt Mélange, rock uplift rates approach 0.5 mm/yr and annual rainfall is 1.2 m , mostly falling between October and April. These factors promote earthflow and landslide activity on long, gently inclined (<35%) hillslopes (Figure 1). Inspection of LiDAR data in this region reveals widespread instability, as the terrain exhibits fluid-like morphology associated with earthflows spanning a range of sizes and activity states [Mackey *et al.*, 2009]. Only a small fraction of these slow-moving features are active [Kelsey, 1978], reflecting the legacy of variations in climate, bedrock weathering, and base-level lowering. While the slides respond to fall and

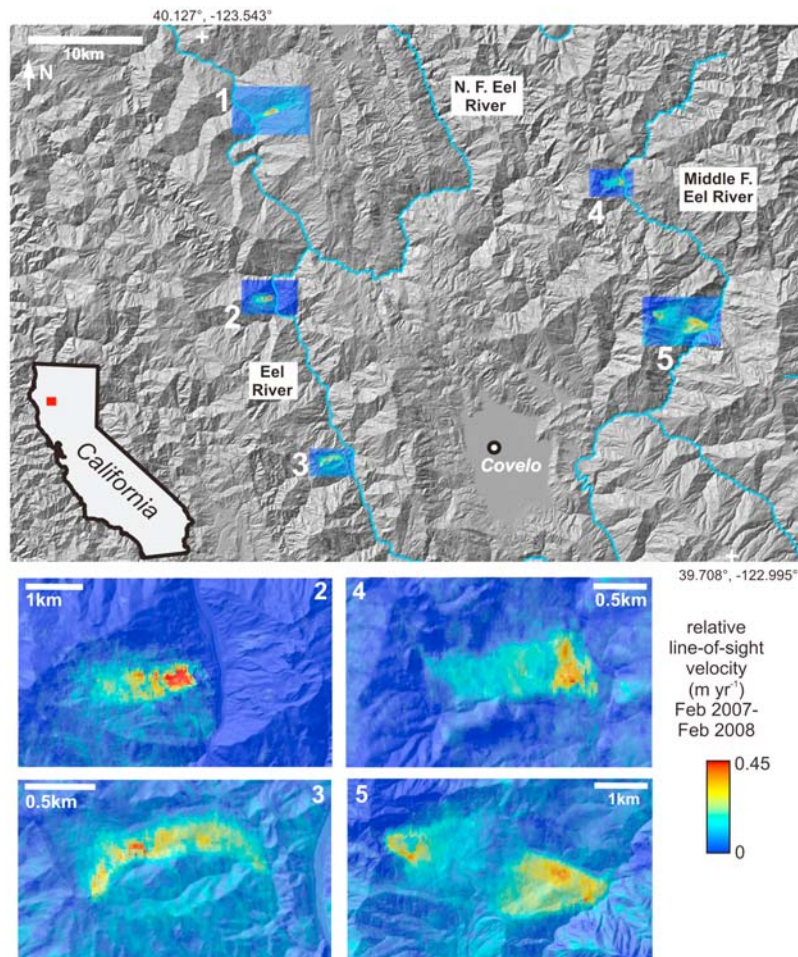


Figure 1. Shaded relief map of the central portion of the Eel River catchment, northern California. Color overlays show large (>1 km), slow-moving landslides identified using 17 stacked ALOS DInSAR interferograms collected from February 2007 to February 2008. Slide 1 is the Boulder Creek earthflow complex (see Figure 2).

winter rainfall events, they do not appear to exhibit catastrophic displacement [Iverson, 1987]. Field observations suggest that these slope failures move essentially via plug flow along discrete shear zones with highly variable rates of transport and sediment delivery [Nolan and Janda, 1995]. During periods of high discharge, rivers transport the predominantly fine-grained products of earthflow translation as suspended load [Kelsey, 1978]. Hillslopes subject to earthflow erosion also tend to experience gullying as discontinuous drainage networks frequently traverse active slides. The role of these gully systems in delivering sediment to major fluvial channels has not been well-quantified.

3. Regional Identification of Active Landslides Using DInSAR

[5] InSAR datasets provide spatially extensive estimates of surface deformation relative to the satellite look direction. Launched in early 2006, the ALOS satellite acquires scenes with a frequency of about 1.5 months at our study site. Data from the ALOS satellite is continually being acquired, but for this contribution we only analyzed imagery acquired from February 2007 to February 2008 to assess the average annual pattern of deformation. We processed 17 interferograms along two adjacent ascending satellite tracks using the Repeat Orbit

Interferometry Package [Rosen *et al.*, 2004]. SAR data were processed at 4 range looks (~ 30 m resolution), and the topographic component of the phase was estimated and removed using a 1-arcsecond SRTM Digital Elevation Model (DEM). Atmospheric artifacts, which are caused by the added delay of the radar signal due to water vapor, are the largest source of error in the interferograms [Zebker *et al.*, 1997]. In order to minimize this source of noise, 17 interferograms along path 224 were stacked by summing the phase for coregistered pixels and dividing by the cumulative time spanned by all interferograms (Table S1).¹ This procedure provides a surface deformation rate averaged over one year.

[6] A reconnaissance-level analysis of stacked interferograms for an 8,400 km² area along the Eel River reveals numerous kilometer-scale zones of focused deformation (Figure 1). The zones of deformation are elongate normal to nearby major channels and typically do not cross-cut ridgelines or neighboring channels, suggesting that these signals primarily reflect landslide-related surface change. The average line-of-sight (LOS) velocities for the five landslides shown in Figure 1 vary between 0.1 and 0.4 m yr⁻¹. Because the satellite's look direction is inclined $\sim 35^\circ$ from

¹Auxiliary materials are available in the HTML. doi:10.1029/2009GL040374.

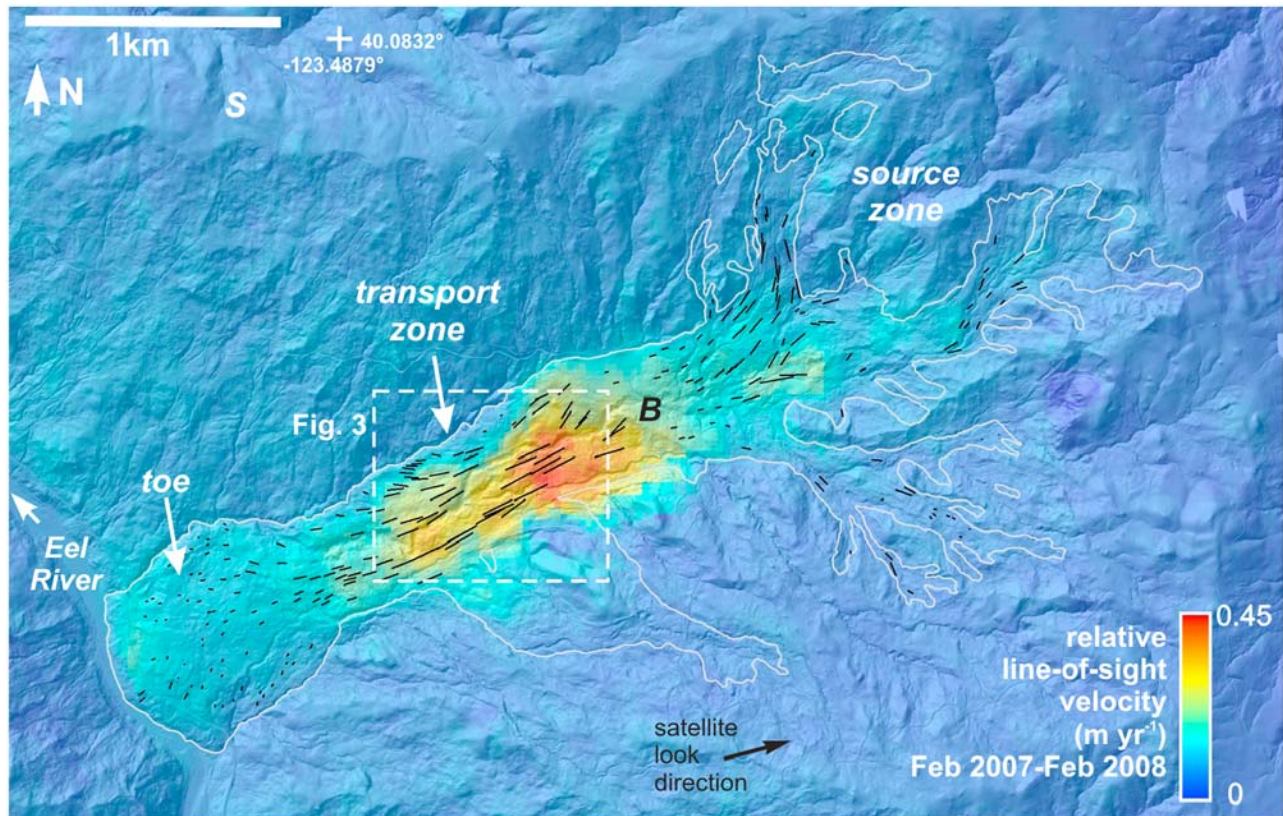


Figure 2. Boulder Creek earthflow (shown as 1 in Figure 1) with LOS velocities (same as Figure 1) atop a shaded relief map derived from airborne LiDAR (~ 1 m spacing). The thin white line denotes the active landslide boundary. Black lines denote the starting and ending location of individual trees mapped on the 1964 air photos and 2006 unfiltered LiDAR DEM. “S” demarcates a patch of stable terrain used to reference DInSAR velocities. “B” denotes a structure or lithology controlled break in slope in the transport zone.

vertical along a horizontal azimuth of 76° clockwise from north, these values cannot be readily interpreted as a downslope velocity.

[7] At least two of these features correspond to previously identified, slow-moving landslides (Boulder Creek and Taliaferro, 1 and 5, respectively, on Figure 1). The Taliaferro landslide is a landslide-rockfall complex that has been mapped and monitored since exhibiting significant deformation in 1996 (J. de la Fuente, USFS, personal communication). The currently active portion of the landslide initiated within the headscarp of a larger landslide complex and has periodically formed and infilled ponds within the landslide body. The Boulder Creek landslide, which exceeds 5 km in length and exhibits classic earthflow morphology with distinct source, transport, and toe regions, has not been subject to systematic study. Focusing on large (>1 km²) features with readily resolved deformation, our reconnaissance analysis demonstrates that $\sim 2\%$ of the region shown in Figure 2 experienced significant movement from February 2007 to February 2008. This is consistent with the notion that the majority of sediment mobilized in slide-prone landscapes emanates from a relatively small proportion of the terrain area.

4. Coupling DInSAR With LiDAR-Derived Topography: Boulder Creek Earthflow

[8] In 2006, NCALM (National Center for Airborne Laser Mapping) acquired a 200 km² airborne LiDAR

DEM processed to 1 m spacing along a section of the Eel River that encompasses the Boulder Creek earthflow. We used the LiDAR DEM to map the landslide boundaries (Figure 2) as well as the location of landslide-channel and landslide-gully interfaces (Figure 3). We used morphologic indicators, including roughened surfaces as well as shear, tensile, and compressional structures, to delineate the active landslide margins. Some terrain outside our mapped landslide boundary exhibits the signature of previous (but currently inactive) slope instability. A relatively large “tributary” earthflow enters the primary transport zone from the south although its level of activity is somewhat ambiguous (Figure 2).

[9] We overlaid the stacked interferograms onto a shaded relief LiDAR image of Boulder Creek and the surrounding terrain (Figure 2) and noted a strong correspondence between our mapped landslide and DInSAR-derived LOS velocities greater than ~ 0.1 m yr⁻¹. Deformation in the branching source zone is non-uniform, consistent with the spatially variable signature of slope deformation revealed by the LiDAR data. Velocities increase where branches of the source zone converge and feed the upper end of the transport zone. Near the upper edge of the transport zone (labeled “B” on Figure 2), a significant break in slope runs obliquely across the earthflow and a zone of increased velocity occurs just downslope, potentially reflecting flow acceleration over a structural or lithologic boundary in the underlying bedrock. LOS velocities within this lower portion of the transport zone, which is heavily dissected by gullies, uniformly exceed

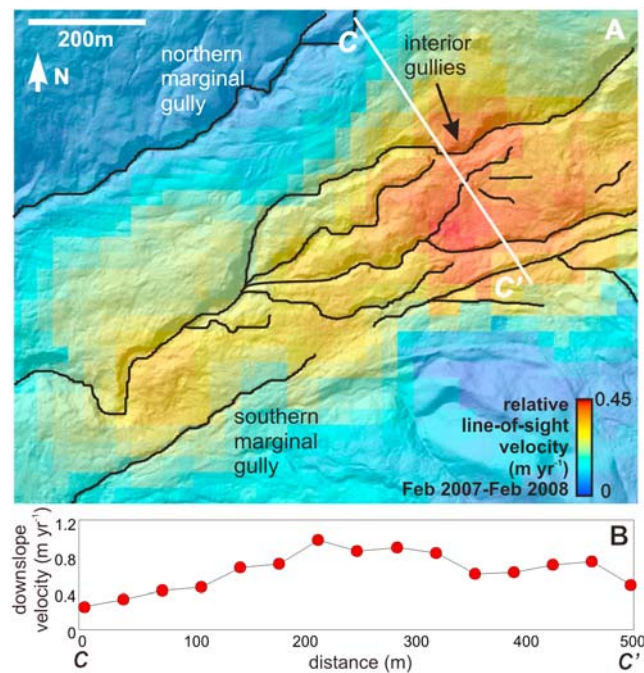


Figure 3. (a) Inset of Figure 2 showing rapid LOS velocities in the transport zone. Thin black lines denote mapped gullies identified from LiDAR DEM. (b) Profile of average downslope velocity inferred from DInSAR along the line C-C' shown in Figure 3a.

0.2 m yr^{-1} and locally eclipse 0.4 m yr^{-1} . The toe of the Boulder Creek earthflow exhibits low rates of deformation apart from a small zone of moderate movement ($\sim 0.2 \text{ m yr}^{-1}$) near the Eel River. Notably, the area of rapid movement in the transport zone does not extend downslope, suggesting that the observed landslide movement does not directly convey that material into the Eel River.

[10] We compared the one-year DInSAR-derived deformation pattern with decadal-scale slide velocities generated through analysis of the LiDAR data and archival air photos. After high accuracy ($< 2 \text{ m}$) ortho-rectification of 1:24,000-scale air photos taken in 1964, we mapped the cumulative displacement of > 100 trees on the landslide surface by comparing their position in the photos and the unfiltered LiDAR data flown in 2006. The thin, black lines (i.e., “tree” vectors) on Figure 2 represent the trajectory of individual trees over 42 years. The resulting displacement pattern is fastest in the transport zone (where it locally exceeds 2 m yr^{-1}) and near the base of the source zone, coincident with areas of rapid movement revealed by our DInSAR analysis. The absence of “tree” vectors in many portions of the landslide does not imply negligible movement, but instead reflects the lack of trees found in both the photos and LiDAR data.

5. Estimating Landslide Velocity and Sediment Transport With DInSAR

[11] Our interferograms resolve only one component of the three-dimensional surface displacement field, namely the component along the satellite’s line-of-sight. Currently, we only have SAR data collected along an ascending orbital trajectory, and therefore we cannot use descending data to

constrain a second deformation component. Instead, we used the tree vectors to infer the orientation of surface displacements on the slide and calculated the displacements required to explain the LOS observations. Along the profile C-C', which is representative of the central transport zone (Figure 3a), we back-projected LOS velocities onto a downslope vector that is oriented parallel to the interpolated tree vector azimuths. From the LiDAR data, we used the local slope angle to infer the vertical component of the unit displacement vector. For this calculation, we down-sampled the LiDAR DEM to a 30-m spacing in order to avoid artifacts associated with local surface roughness. Because DInSAR measures relative phase shifts, we referenced LOS velocities to a patch of stable terrain about 2 km north-northwest of the transport zone (see ‘S’ on Figure 2). Consistent with the LOS and air photo-derived velocity fields, downslope velocities are highest through the central and southern portions of the transport zone (Figure 3b). In this zone of rapid displacement, velocities uniformly exceed 0.7 m yr^{-1} and are slightly lower than the decadal values generated by the air photo-LiDAR procedure (Figure 2).

[12] To estimate the downslope flux of sediment through the transport zone, we obtained minimum estimates of the earthflow depth by measuring the depth of gully incision into the earthflow (Figure 3a). Depths vary between 8 and 12 meters, similar to the depth of previously instrumented earthflows in the region [Iverson, 1987; Nolan and Janda, 1995]. By integrating our depth estimates along the C-C' velocity profile, we calculated the minimum volumetric sediment flux through the transport zone to be $4100 \pm 800 \text{ m}^3 \text{ yr}^{-1}$. Given the upslope area of the Boulder Creek earthflow surface (2.5 km^2) and the negligible upslope propagation of the source zone over the time period of our analysis, this yields a minimum lowering rate of $1.6 \pm 0.4 \text{ mm yr}^{-1}$. This lowering rate falls above the upper end of erosion rates (0.1 to 1.5 mm yr^{-1}) previously estimated for the Eel River basin from suspended sediment data [Brown and Ritter, 1971], highlighting the highly erosive and transient nature of these large, slow-moving landslides [Mackey et al., 2009].

[13] As noted above, areas of fast movement in the transport zone do not directly convey material into the Eel River. To analyze the role of gullies in facilitating sediment conveyance into the fluvial network, we used the LiDAR DEM to map the distribution of gullies through the central portion of the landslide (Figure 3a) and noted that the region of rapid transport corresponds with an area of anomalously high gully density. Downslope, these gullies diverge around the outer margins of the earthflow toe and enter the Eel River (Figure 2). In the field, the gully walls tend to be steep and abundant, unvegetated sediments on the channel bed suggest recent activity. Also, comparison of gully locations in the 1964 air photos and 2006 LiDAR data reveals localized, yet substantial ($> 5 \text{ m}$) lateral gully migration. The association of fast slide movement with dense, dynamic gullies in the central portion of the landslide suggests a process coupling that may efficiently transmit landslide-derived sediment into the fluvial network despite negligible movement of the toe region.

6. Discussion and Conclusions

[14] The framework we propose should allow for the documentation of temporal and spatial variations in landslide-

driven sediment production at the drainage basin scale, although some DInSAR systematics regarding terrain aspect and steepness require further investigation. Because rivers generally parallel the north–south structural grain of the northern California Coast Range [McLaughlin et al., 1982], large earthflow complexes connected to major channels tend to move in the east or west direction. Given the look direction of the ALOS satellite (see Figure 2), this landscape configuration maximizes the likelihood that deformation will be accurately resolved [Squarzoni et al., 2003].

[15] An alternative to our technique of using historical air photos to constrain DInSAR displacement orientations is to assume that slide movement proceeds downslope according to local topography. Although simple in principle, this endeavor yields highly variable results depending on the topographic grid spacing (i.e., DEM resolution) used to calculate the local gradient vector. On large landslides, for example, hummocky terrain of varying scale can lead to erroneous prediction of landslide movement direction. Alternatively, acquisition of ascending and descending track SAR data will allow for accurate characterization of landslide displacements [Catani et al., 2005].

[16] Our analysis demonstrates the potential of coupled ALOS interferometry and airborne LIDAR for resolving the details of active earthflows and subsidiary processes and documents the first imagery of active landsliding in the vegetated, mountainous terrain of northern California. Several characteristic features of earthflows are revealed, including variable rates of movement and convergence in the source region and velocities that depend on underlying structural or lithologic controls. Assuming that the slope break cutting across the transport zone of the earthflow persists [Coe et al., 2009], continued movement in the source zone will translate sediment across that feature and into the rapidly moving transport zone. Our results are consistent with previous studies which suggest that large landslide displacements can set the stage for small-scale mass wasting processes, such as debris flows, to deliver sediment to channel networks [Malet et al., 2005; Schwab et al., 2008]. Notably, our methodology highlights the importance of gullies, which are only resolvable with high-resolution airborne LiDAR, for transferring earthflow-generated material into the Eel River. The correspondence between a highly dissected zone of active gullies and a region of rapid earthflow movement may reflect a first-order process coupling that drives the long-term evolution of individual landslides. Consistent with the interpretations of Kelsey [1978], the large, active landslides imaged here constitute a small fraction of our study area and occur on relatively gentle slopes, yet likely account for a substantial fraction of landscape denudation.

[17] **Acknowledgments.** JJR and DAS received financial support from NASA (NNX08AF95G). UO computational resources funded by NSF (EAR-0651123). Comments by two anonymous reviewers greatly improved a previous version of the manuscript.

References

- Baum, R. L., et al. (1998), Surface deformation as a guide to kinematics and three-dimensional shape of slow-moving, clay-rich landslides, Honolulu, Hawaii, *Environ. Eng. Geosci.*, *4*, 283–306.
- Brown, W. M., and J. R. Ritter (1971), Sediment transport and turbidity in the Eel River basin, California, *U.S. Geol. Surv. Water Supply Pap.*, *1986*, 67.
- Bulmer, M. H., D. N. Petley, W. Murphy, and F. Mantovani (2006), Detecting slope deformation using two-pass differential interferometry: Implications for landslide studies on Earth and other planetary bodies, *J. Geophys. Res.*, *111*, E06S16, doi:10.1029/2005JE002593.
- Catani, F., et al. (2005), On the application of SAR interferometry to geomorphological studies: Estimation of landform attributes and mass movements, *Geomorphology*, *66*, 119–131, doi:10.1016/j.geomorph.2004.08.012.
- Chandler, J. H., and D. Brunsten (1995), Steady state behaviour of the Black Ven mudslide: The application of archival analytical photogrammetry to studies of landform change, *Earth Surf. Processes Landforms*, *20*, 255–275, doi:10.1002/esp.3290200307.
- Coe, J., et al. (2009), Basal-topographic control of stationary ponds on a continuously moving landslide, *Earth Surf. Processes Landforms*, *34*, 264–279, doi:10.1002/esp.1721.
- Delacourt, C., et al. (2007), Remote-sensing techniques for analysing landslide kinematics: a review, *Bull. Soc. Geol. Fr.*, *178*, 89–100, doi:10.2113/gssgfbull.178.2.89.
- Guzzetti, F., et al. (2009), Landslide volumes and landslide mobilization rates in Umbria, central Italy, *Earth Planet. Sci. Lett.*, *279*, 222–229.
- Hilley, G. E., et al. (2004), Dynamics of slow-moving landslides from permanent scatterer analysis, *Science*, *304*, 1952–1955, doi:10.1126/science.1098821.
- Hovius, N., et al. (1997), Sediment flux from a mountain belt derived by landslide mapping, *Geology*, *25*, 231–234, doi:10.1130/0091-7613(1997)025<0231:SFFAMB>2.3.CO;2.
- Iverson, R. M. (1987), Rainfall, ground-water flow, and seasonal movement at Minor Creek landslide, northwestern California: Physical interpretation of empirical relations, *Geol. Soc. Am. Bull.*, *99*, 579–594, doi:10.1130/0016-7606(1987)99<579:RGFASM>2.0.CO;2.
- Kelsey, H. M. (1978), Earthflows in Franciscan melange, Van Duzen River basin, California, *Geology*, *6*, 361–364.
- Kelsey, H. M. (1987), Geomorphic processes in the recently uplifted coast ranges of northern California, in *Geomorphic Systems of North America*, edited by W. L. Graf, pp. 550–560, Geol. Soc. of Am., Denver, Colo.
- Korup, O., et al. (2007), Giant landslides, topography, and erosion, *Earth Planet. Sci. Lett.*, *261*, 578–589, doi:10.1016/j.epsl.2007.07.025.
- Mackey, B., et al. (2009), Long-term kinematics and sediment flux of an active earthflow, Eel River, California, *Geology*, *37*, 803–806.
- Malet, J.-P., et al. (2002), The use of Global Positioning System for the continuous monitoring of landslides: Application to the Super-Sauze earthflow (Alpes-de-Haute-Provence, France), *Geomorphology*, *43*, 33–54, doi:10.1016/S0169-555X(01)00098-8.
- Malet, J.-P., et al. (2005), Triggering conditions and mobility of debris flows associated to complex earthflows, *Geomorphology*, *66*, 215–235, doi:10.1016/j.geomorph.2004.09.014.
- Massonnet, D., and K. L. Feigl (1998), Radar interferometry and its application to changes in the Earth's surface, *Rev. Geophys.*, *36*, 441–500.
- McLaughlin, R. J., et al. (1982), Post-middle Miocene accretion of Franciscan rocks, northwestern California, *Geol. Soc. Am. Bull.*, *93*, 595–605, doi:10.1130/0016-7606(1982)93<595:PMAOFR>2.0.CO;2.
- Nolan, K. M., and R. J. Janda (1995), Movement and sediment yield of two earthflows, northwestern California, in *Geomorphic Processes and Aquatic Habitat in the Redwood Creek Basin, Northwestern California*, edited by K. M. Nolan et al., *U. S. Geol. Surv. Prof. Pap.*, *1454-F*, F1–F12.
- Rosen, P. A., et al. (2004), Updated repeat orbit interferometry package released, *Eos Trans. AGU*, *85*, doi:10.1029/2004EO050004.
- Sandwell, D. T., et al. (2008), Accuracy and resolution of ALOS interferometry: Vector deformation maps of the Father's Day intrusion at Kilauea, *IEEE Trans. Geosci. Remote Sens.*, *46*, 3524–3534, doi:10.1109/TGRS.2008.2000634.
- Schwab, M., et al. (2008), Landsliding and sediment flux in the Central Swiss Alps: A photogrammetric study of the Schimbrig landslide, Entlebuch, *Geomorphology*, *97*, 392–406, doi:10.1016/j.geomorph.2007.08.019.
- Slatton, K. C., W. E. Carter, R. L. Shrestha, and W. Dietrich (2007), Airborne laser swath mapping: Achieving the resolution and accuracy required for geosurficial research, *Geophys. Res. Lett.*, *34*, L23S10, doi:10.1029/2007GL031939.
- Squarzoni, C., et al. (2003), Nine years of spatial and temporal evolution of the La Valette landslide observed by SAR interferometry, *Eng. Geol.*, *68*, 53–66, doi:10.1016/S0013-7952(02)00198-9.
- Zebker, H. A., P. A. Rosen, and S. Hensley (1997), Atmospheric effects in interferometric synthetic aperture radar surface deformation and topographic maps, *J. Geophys. Res.*, *102*, 7547–7563, doi:10.1029/96JB03804.

B. H. Mackey, J. J. Roering, D. A. Schmidt, and L. L. Stimely, Department of Geological Sciences, University of Oregon, Eugene, OR 97403-1272, USA. (jroering@uoregon.edu)